

Measurements of Turbulent Transport in a Square Channel With One Ribbed Wall

Sebastian Ruck¹

Institute for Neutron Physics and
Reactor Technology,
Measurement Technology and
Experimental Methods,
Karlsruhe Institute of Technology,
Hermann-von-Helmholtz-Platz 1,
Eggenstein-Leopoldshafen 76344, Germany
e-mail: sebastian.ruck@kit.edu

Frederik Arbeiter

Institute for Neutron Physics and
Reactor Technology,
Measurement Technology and
Experimental Methods,
Karlsruhe Institute of Technology,
Hermann-von-Helmholtz-Platz 1,
Eggenstein-Leopoldshafen 76344, Germany
e-mail: frederik.arbeiter@kit.edu

The velocity field of the fully developed turbulent flow in a one-sided ribbed square channel (rib-height-to-channel-height ratio of $k/h = 0.0667$ and rib-pitch-to-rib-height ratio of $p/k = 9$) was measured at Reynolds numbers (based on the channel height h and the mean bulk velocity u_B) of $Re_h = 5.0 \times 10^4$ and 1.0×10^5 by means of laser Doppler anemometry (LDA). Triple velocity correlations differed slightly between both Reynolds numbers when normalized by the bulk velocity and the channel height, similarly to the first- and second-order statistical moments of the velocity. Their near-wall behavior reflected the crucial role of turbulent transport near the rib crest and within the separated shear layer. Sweep events occurred with the elongated flow structures of the flapping shear layer and gained in importance toward the channel bottom wall, while strong ejection events near the rib leading and trailing edges coincided with flow structures bursting away from the wall. Despite the predominant occurrence of sweep events close to the ribbed wall within the inter-rib spacing, ejection events contributed with higher intensity to the Reynolds shear stress. Ejection and sweep events and their underlying transport phenomena contributing to the Reynolds shear stress were almost Reynolds number-insensitive in the resolved flow range. The invariance to the Reynolds number can be of benefit for the use of scale-resolving simulation methods in the design process of rib structures for heat exchange applications.

1 Introduction

Turbulent flow in cooling channels of noncircular cross section with one- or two-sided ribbed channel walls is of high engineering importance to heat exchange applications with high-temperature interfaces, including internal cooling channels of turbine blades, gas-cooled reactor components, or solar receivers [1–4]. For that reason, turbulent flow in rectangular ducts of moderate aspect ratios with a width w and height h or square channels roughened by transverse ribs of height k , width b , and pitch p has been the subject of research for decades. The rib roughness provides an effective fluid mixing for channel flows, and numerous studies analyzing the effect of rib-pitch-to-rib-height ratio (p/k) [5,6], the relative roughness (k/h) [7,8], the unsteady flow motion [9–15], and the thermal flow field [16–18] for Reynolds numbers (based on the channel height h and the mean bulk velocity u_B) of the order of magnitude of $O(10^3)$ and $O(10^5)$ have been carried out so far.

The flow field in ribbed square channels is highly three-dimensional. Viscous effects from the wall-bounded shear layers of the lateral sidewalls as well as strong secondary flows of the first and second kind affect the flow field and lead to difference compared to two-dimensional flow configurations. The near-rib flow field is dominated by secondary flow motion, vortex shedding, shear layer separation, reattachment, and boundary layer recovery within the inter-rib spacing, as sketched in Fig. 1 within the channel center plane of ribbed square or rectangular channels. At the windward rib surface, the flow is deflected laterally and upwards by the rib blockage. Due to the lateral and upward displacement and the associated pressure change along the rib [19], a three-dimensional secondary flow developed. It is represented in the time average by a vortex system consisting of two large counter-rotating vortices with rotational axes oriented in the main flow direction. This is evident from the hot wire measurements

in one- and two-sided ribbed square channels ($p/k = 10$ and $k/h = 0.02$) carried out at a Reynolds number of $Re_h = 6.5 \times 10^4$ by Yokosawa et al. [20], Fujita et al. [21], and Hirota et al. [22]. The upwards deflected fluid streams against the downwards directed mean flow driven by the secondary flow at upper channel half. At the rib leading edge, flow detaches due to the pressure gradient between the rib crest and the windward rib surface and reattaches on the rib crest forming a small recirculation bubble. A high density of vortex structures in the region of the leading rib roof indicates that the detachment and reattachment processes are continuous [13]. Occasionally, packets of rotational fluid, located near the rib leading edge, are ejected into the channel core flow [23]. The fluid acceleration above the rib causes high mean velocities which results in a steep rise of the mean shear rates and in a Reynolds stresses increase. The direct numerical simulation result by Mahmoodi-Jezeh and Wang [8] for ribbed channel flows with rectangular and square ribs ($k/h = 0.05, 0.1$, and 0.2) at a Reynolds number of $Re_h = 5.6 \times 10^3$ as well as the particle image velocimetry (PIV) results by Casarsa and Arts [9] for turbulent flow in a square channel with a high relative roughness ($p/k = 10$ and $k/h = 0.3$) at a Reynolds number of $Re_h = 4.0 \times 10^4$ revealed that the maximum streamwise Reynolds normal stress occurs at the rib crest and originates in the strong mean shear rate of the attached shear layer. Among all others, the streamwise Reynolds normal stress is the highest. Peaks of the vertical Reynolds normal stress and Reynolds shear stress in the proximity of the rib leading edge were found by several authors [10,13,15,17]. Wang et al. [10] carried out PIV measurements in a

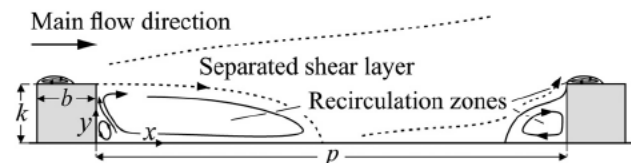


Fig. 1 Sketch of the near-wall mean flow field within the channel center plane in a ribbed square channel

¹Corresponding author.

ribbed square channel ($p/k = 10$ and $k/h = 0.2$) at a Reynolds number of $Re_h = 2.2 \times 10^4$. Their results showed that the Reynolds shear stress increase at the rib leading edge is mainly driven by ejection events.

The intense attached shear layer above the rib crest grows along the rib crest and separates at the rib trailing edge. The adverse pressure gradient due to the sudden cross section expansion deflects the fluid toward the ribbed channel wall. The shear layer reattaches on the channel wall within the inter-rib spacing, and a spacious recirculation region develops beneath the separated shear layer. The mean reattachment length of the shear layer depends on the height and width of square ribs and the Reynolds number as shown by experimental studies of turbulent flow in ribbed rectangular ducts and square channels by Rau et al. [6], Ruck and Arbeiter [15], and Islam et al. [24]. Maximum Reynolds shear stress occurs within the separated shear layer [25,26], and peaks of Reynolds normal stress in wall normal direction occur in the border region between the separated shear layer and the recirculation region and at the rib leading edge [13,15]. The intense primary mean velocity shear in the streamwise flow direction and the elevated Reynolds shear stresses within the separated shear layer form the dominant production term for the Reynolds normal stresses, which is reflected in a developed anisotropy of the turbulent fluctuation field in the rib wake flow. Wang et al. [26] measured the turbulent flow structures of separated flow in a channel with square ribs ($p/k = 12$ and $k/h = 0.15$) applied to one wall at a Reynolds number of $Re_h = 2.2 \times 10^4$ by PIV. The results showed that the separated shear layer is dominated by vortices which develop during the roll-up process of the shear layer formation. Longitudinal and lateral Taylor microscales, derived from the corresponding autocorrelation profiles, indicate anisotropy of the turbulence field which increases with increasing wall distance. The strongly anisotropic distribution of Reynolds stresses occurs for rib roughnesses of different relative roughness [9,27] and was discussed to be one of the driving forces for the formation and intensification of secondary flows in ribbed channels [21,25].

The wake is highly unsteady and is governed by flapping of the shear layer and the intermittent motion of vortex structures of the recirculation region, as reflected in the sharp and bimodal frequency diagrams of its velocity fluctuations [10]. Large-scale flow structures, which are generated from the shear layer formation and separation, persist along the entire inter-rib spacing while moving downstream and characterize the flow impingement on the successive rib where they participate again in the flow structure generation and shedding. This is shown by Coletti et al. [13], who carried out PIV measurements in a square channel with square ribs ($p/k = 10$ and $k/h = 0.1$) on one wall at a Reynolds number of $Re_h = 1.5 \times 10^4$. By means of time-accurate flow visualization in a two-sided oppositely ribbed square channel with square ribs ($p/k = 8$ and $k/h = 0.12$), Cardwell et al. [11] identified burst events behind the rib trailing edge, which originate in the recirculation region causing a rapid fluid ejection into the core flow. The ejected flow structures can travel through the channel core before they diffuse. Shear layer thickness and height as well as the size

of the large-scale flow structures grow in streamwise direction [26]. In the postreattachment region, a new attached shear layer develops which detaches in front of the subsequent rib forming a small recirculation region. Similarly to rough turbulent boundary layer flows [28–31] and flows in channels with two-dimensional roughnesses [32,33], the channel roughness significantly affects the turbulent transport mechanism. As shown for turbulent flow in rib-roughened square channels [8,15], turbulent diffusion and mean convection contribute significantly to the turbulence kinetic energy (TKE) budget near the rib causing the occurrence of a non-equilibrium TKE layer above the ribs. A production–dissipation equilibrium establishes above the location where turbulent diffusion and mean convection vanished.

1.1 Objective. Even though turbulent flows over walls roughened by transverse ribs have been investigated intensively, only a very limited number of experimental studies reporting high-order statistical moments in ribbed square channels at Reynolds numbers relevant to high-temperature cooling applications have been performed. Therefore, flow physics and turbulent transport mechanisms remain still unclear in some points, and detailed data enabling a validation of computations and turbulence models for calculating turbulent flow in ribbed square or rectangular channels at high Reynolds numbers are lacking. This study investigates the turbulent transport in a one-sided ribbed square channel at Reynolds numbers of $Re_h = 5.0 \times 10^4$ and 1.0×10^5 by means of high-order statistical moments which were determined from laser Doppler anemometry (LDA) velocity measurements in the fully developed flow regime. Turbulent transport mechanisms are discussed by distributions of triple velocity correlations and quadrant analysis. The corresponding first- and second-order moments of the velocity have been examined in detail in a companion study [15]. Furthermore, the results provide a basis for computational method and turbulence model validation.

2 Experimental Facility and Methodology

Measurements were conducted in a closed air loop test facility. It contained a test section, an entrance channel, a Coriolis mass flowmeter as well as pressure and thermal measurement devices, as illustrated in Fig. 2(a). The constant mass flow rate \dot{m} was provided by four side channel blowers. The height and width of the square test section and the entrance channel were 60 mm. The length of the entrance channel was 3056 mm. A flow straightener and two honeycomb grids for reducing vortical and large-scale flow structures were installed at the entrance channel inlet. The air flow was tripped by a thin wire immediately downstream the honeycomb grid to accelerate the turbulent flow development. The test section contained a smooth inlet zone and the ribbed test zone. The length of the test section was 1180 mm. The channel bottom wall of the test zone was roughened by 27 square ribs with a rib height and width of $k = b = 4$ mm and a pitch of $p = 36$ mm. The blockage ratio was $k/h = 0.0667$. The

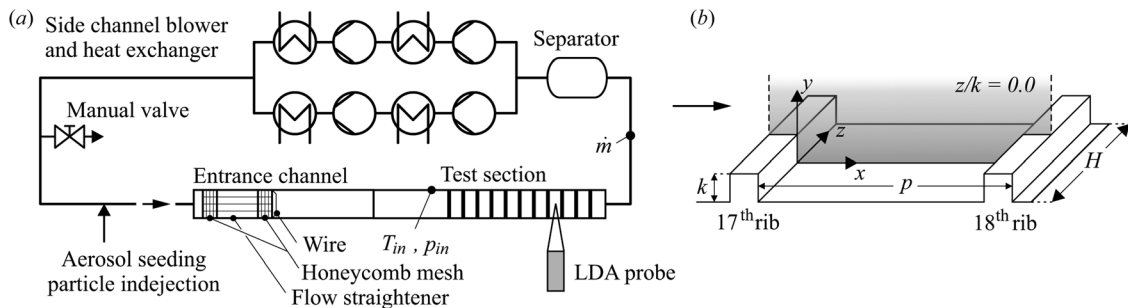


Fig. 2 Sketch of (a) the experimental setup and of (b) the rib configuration and measurement plane (channel center plane). The origin of the Cartesian coordinate system (x, y, z) was located at the leeward surface of the 17th rib and the channel bottom wall.

rib-roughened channel bottom was made of black polyamide with a surface roughness of $Ra = 1.0\mu\text{m}$. The optical access for the LDA measurements was provided by windows of homogeneous silica Spectrosil glass at the sidewalls of the test section.

The velocity in streamwise (x -) direction (u) and in vertical (y -) direction (v) were measured with a Dantec Dynamics fiber optical LDA system operating in the backscatter mode. A Spectra-Physics air-cooled 320 mW Ar-ion laser provided beams of 488 nm and 514.5 nm wavelength. It contained a Bragg cell for the frequency shift. Both beams were routed through optical cables to a two-component 60 mm FiberFlow LDA probe with a 160 mm focal length lens. The measurement volume diameter and length were $78\mu\text{m}$ and $658\mu\text{m}$ (u) and $74\mu\text{m}$ and $625\mu\text{m}$ (v), respectively. The LDA probe was mounted sideways the test section on a movable three-axis Newport traverse system with a $\pm 10\mu\text{m}$ resolution. The flow was seeded by di-ethyl-hexyl-sebacat aerosol, which was generated by a Topas ATM 210/H particle generator and injected into the test facility upstream the entrance channel. The increase in the mass flow rate and in the operating pressure by the overpressure injection of the di-ethyl-hexyl-sebacat aerosol seeding particles was controlled by the manual valve.

As shown by Graham et al. [7] and Sewall et al. [16], turbulence quantities in rib-roughened square channels are fully developed after a development length $x/H \geq 10$. Therefore, velocities were measured between the 17th and 18th ribs within the channel center plane ($z/k = 0.0$) as depicted in Fig. 2(b). A comparison with mean velocities and Reynolds stresses measured between the 18th and 19th ribs revealed deviations less than the measurement uncertainty indicating the flow field periodicity and the fully developed flow conditions within the measurement region.

Velocities were measured in the burst acquisition mode. Since the sample rate decreased with decreasing wall distance, the sample number per measurement point was varied with the wall distance to keep the measuring time per measurement point within reasonable limits: The minimum was 5.0×10^4 samples very close to the ribbed wall and 2.0×10^5 samples within the channel core region, respectively. Due to the measurement volume configuration, the wall-closest measurement point where burst signals were detected was set to a wall distance of 0.08 mm. A Dantec Dynamics BSA Flowmaster P80 was used for the signal processing. The LDA measuring process, the data transfer, and the traverse system were controlled with the BSA FLOW SOFTWARE 6.5. For each LDA measurement run at one measurement location, the inlet temperature (T_{in}) and inlet pressure (p_{in}) upstream the ribbed test zone and the mass flow rate (\dot{m}) downstream the test section were time-averaged over the LDA acquisition time and additionally recorded. Due to geometrical and measurement technical constraints, the simultaneous measurement of two-dimensional velocity profiles by LDA was restricted to a region of $1 \leq y/k \leq 9$.

3 Results

The results presented in Figs. 3–7 were normalized with the bulk velocity u_B and the rib height k . A residence time-weighted average [34] is indicated by the symbol $\langle \rangle$ and a fluctuation of an instantaneous value about its mean is labeled by the symbol $'$, e.g., $u' = u - \langle u \rangle$. For the sake of clarity, only 40–50% of the measurement points were shown, and therefore each value for a specified location in the presented plots was averaged over a sliding window of three values centered at the value itself. For a better interpretation of the measurement results, a sketch of the mean flow field features was inserted to the plots. It is based on the distribution of first- and second-order moments (for more details, see Ref. [15]) and must be considered as a rough estimate of the mean flow.

Uncertainty: Stochastic and measuring system errors determined the uncertainty of the time-averaged quantities. The stochastic errors based on the 95% confidence levels with sampling variances determined under the assumption of Gaussian

distributed samples. The mean uncertainty of the Reynolds number was ± 1200 at $Re_\eta = 5.0 \times 10^4$ and ± 2200 at $Re_\eta = 1.0 \times 10^5$. The sampling variances for the triple velocity correlations were determined by estimators given in Ref. [35] at each measurement location. Here, the residence time weighting was applied for calculating the high-order moments, and statistically independent samples were expected to occur after two times the integral time scale [36], which corresponds to two times the area under the normalized temporal autocorrelation function up to the first zero-crossing. The mean uncertainties for the triple velocity correlations are given in the figure captions.

3.1 Triple Velocity Correlations. In Figs. 3 and 4, the triple velocity correlation $\langle u'^3 \rangle$, $\langle v'^3 \rangle$, $\langle u'^2 v' \rangle$, and $\langle u' v'^2 \rangle$ profiles in the vertical direction are depicted. Similarly to the flow in a one-sided ribbed two-dimensional channel at lower Reynolds numbers [37], the normalized distributions showed the same trends for both Reynolds numbers. Local deviations were certainly attributable to the sensitivity of triple correlations to measurement uncertainties and statistical convergence. The triple velocity correlations altered enormously in streamwise and vertical direction within a layer of $1.0 \cdot k$ to $2.0 \cdot k$ height above the rib indicating a large rate of diffusional transport in vertical direction. These findings were in accordance with the occurrence of a nonequilibrium TKE layer in the region $y/k < 3.0$ reported for two-dimensional and three-dimensional ribbed channel configurations [8,15,33]. Under consideration of the measurement uncertainty of the triple velocity correlations, it can be assumed that above the range $3.0 < y/k < 4.0$, the presented distributions became nearly independent of the streamwise position. The triple velocity correlations decreased with increasing wall distance until they had vanished at around $y/k = 9.0$.

The spatial gradients of the triple velocity correlations correspond to the turbulent diffusion of Reynolds stresses and TKE. The large positive $\langle u'^3 \rangle$ values in the vicinity of $y/k = 1.0$ reflected the intense transport of $\langle u'^2 \rangle$ by u fluctuations and were attributed to the vortical motion of streamwise-elongated flow structures which shed from the rib as described by Fang et al. [27]. As reported by Keirsbulck et al. [30] for rough-wall turbulent boundary layers, $\langle u'^3 \rangle > 0$ indicated the distinct occurrence of sweep events conveying high-momentum fluid wallwards into the cavity. This is consistent with the direct numerical simulation results by Mahmoodi-Jezeh and Wang [8] who referred the oppositely signed values of $\langle u'^3 \rangle$ and $\langle v'^3 \rangle$ behind the rib to a shear layer flapping that results in intense sweeps. The turbulent transport that originated in vortex shedding from the rib trailing edge persisted along the entire inter-rib spacing and decreased toward the subsequent rib where the vortical flow structures diffused or impinged as it can be inferred from the decreasing $\langle u'^3 \rangle$ values in streamwise direction. The local minima of $\langle u'^3 \rangle$ at $x/k = 0.1$ and 1.0 slightly above the separated shear layer were referred to vortical structures formed by the shear layer roll-up process and ejected outwards, while the shear layer broke up intermittently as reported by Cardwell et al. [11]. The positive values of $\langle u'^3 \rangle$ and $\langle v'^3 \rangle$ immediately above the rib leading edge indicated an enhanced outward interaction of the Reynolds stresses. The triple correlation $\langle v'^3 \rangle$ crosses zero within the inter-rib spacing below the rib height, and above $y/k = 1.0$, an outwards transport of $\langle v'^2 \rangle$ by vertical fluctuations with the flapping shear layer occurred. Considering Figs. 3(b) and 4(a), it is obvious that the contribution from diffusional transport to TKE at the rib leading edge was large from both $\langle v'^3 \rangle$ and $\langle u'^2 v' \rangle$. Both contributed to the term of the TKE diffusion which is associated with the vertical velocity fluctuation. The positive deviations of $\langle v'^3 \rangle$ and $\langle u'^2 v' \rangle$ within a small layer with a height of $0.5 \cdot k$ above the rib indicate the direction of turbulent diffusion away from the wall causing a loss in the TKE budget. Outside the close range above the rib, the vertical gradients of $\langle v'^3 \rangle$ and $\langle u'^2 v' \rangle$ decreased, and thus the contribution to TKE decreased. The $\langle u'^2 v' \rangle$ and $\langle u' v'^2 \rangle$ curves in Fig. 4

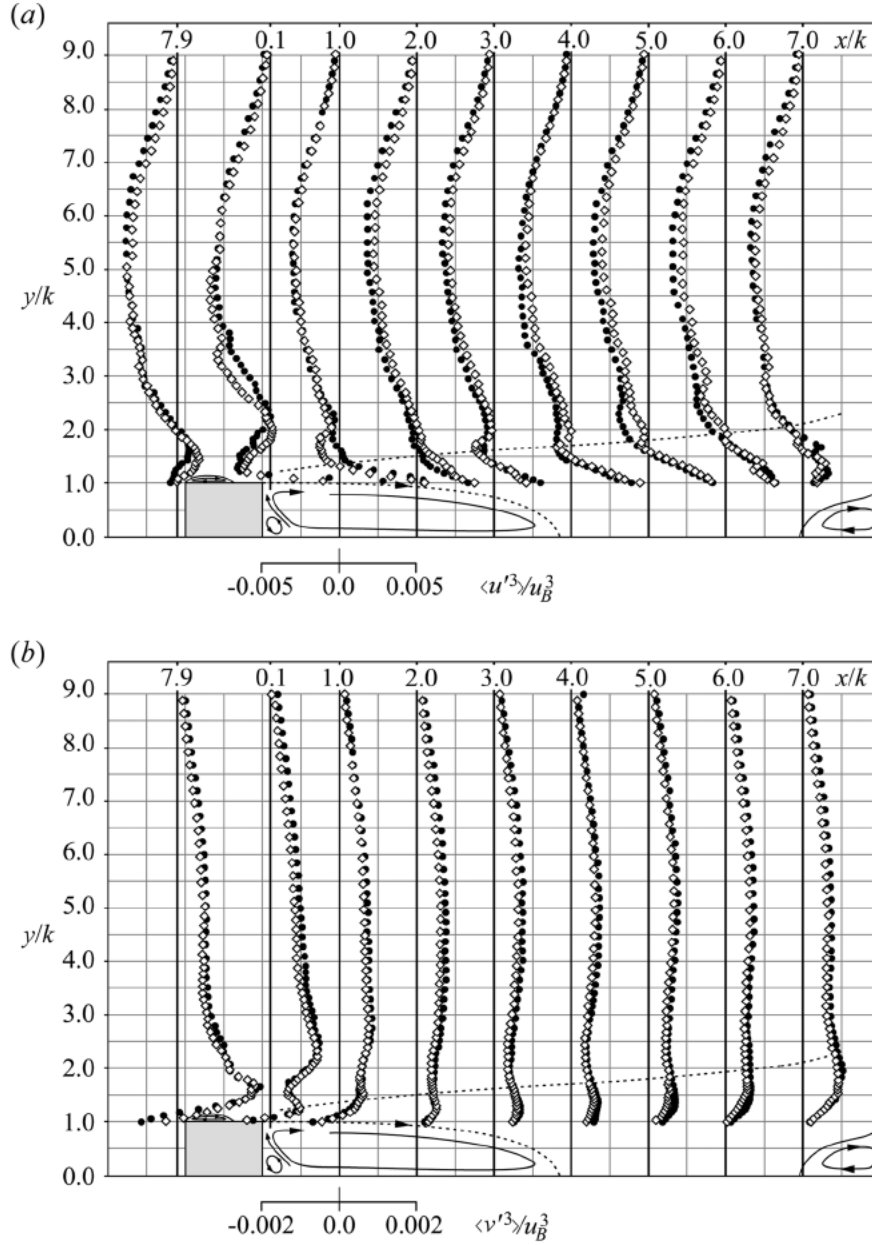


Fig. 3 Normalized triple velocity correlations: (a) $\langle u'^3 \rangle$ and (b) $\langle v'^3 \rangle$: $\diamond Re_h = 5.0 \times 10^4$ and $\bullet Re_h = 1.0 \times 10^5$. Mean uncertainty in $\langle u'^3 \rangle / u_B^3$: ± 0.00034 and ± 0.00039 and in $\langle v'^3 \rangle / u_B^3$: ± 0.00008 and ± 0.00009 for $Re_h = 5.0 \times 10^4$ and 1.0×10^5 .

exhibited similar behavior but with opposite signs. The distribution of $\langle u'^2 v' \rangle \langle (u' v'^2) \rangle$ was almost entirely positive (negative) above the rib leading and trailing edges. A huge peak of $\langle u'^2 v' \rangle \langle (u' v'^2) \rangle$ was located slightly above the rib trailing edge within the separated shear layer at $y/k = 1.35$ yielding a steep positive (negative) vertical gradient. The change of sign in the vertical gradients indicated a turbulent diffusion flux reversal. Further downstream, local maxima (minima) of $\langle u'^2 v' \rangle \langle (u' v'^2) \rangle$ decreased while they drifted outwards, and the positive (negative) vertical gradients declined. Above the global and local peaks of $\langle u'^2 v' \rangle \langle (u' v'^2) \rangle$, the vertical gradients became negative (positive) and, after reaching local minima (maxima), became positive (negative) again. Additional local maxima (minima) occurred in the region between $y/k = 5.0$ and 6.0 and $\langle u'^2 v' \rangle \langle (u' v'^2) \rangle$ converged to zero with increasing wall distance. Negative (positive) values of $\langle u'^2 v' \rangle \langle (u' v'^2) \rangle$ appeared slightly above $y/k = 1.0$ in the range from $x/k = 0.1$ to 6.0 .

The increase in $\langle u'^2 v' \rangle \langle (u' v'^2) \rangle$ near the rib implies a turbulent transport with large-scale eddies that shed from the ribs [37]. Since the triple velocity correlations $\langle u'^2 v' \rangle$ and $\langle u' v'^2 \rangle$ can be attributed to the vertical flux of $\langle u'^2 \rangle$ and $-\langle u' v' \rangle$, the zero-crossing of $\langle u'^2 v' \rangle$ and $\langle u' v'^2 \rangle$ defines a demarcation line between upward and downward mean turbulent transport of the Reynolds stresses. Starting close to the rib trailing edge, the line slightly ascended further downstream. The corresponding Reynolds stress flux was directed toward the bottom wall below the line and outwards above the line. The downward directed transport of $-\langle u' v' \rangle$ by v fluctuations was restricted to a region within the inter-rib spacing. Since the vertical fluctuations are the most relevant for the turbulent heat flux near walls and the streamwise-vertical Reynolds shear stress correlates strongly with the local heat transfer in ribbed square channels [9], it is obvious that turbulent transport is significant for the thermal exchange of fluid near the ribs. Within the inter-rib spacing behind the rib, $\langle u'^2 v' \rangle < 0$ and

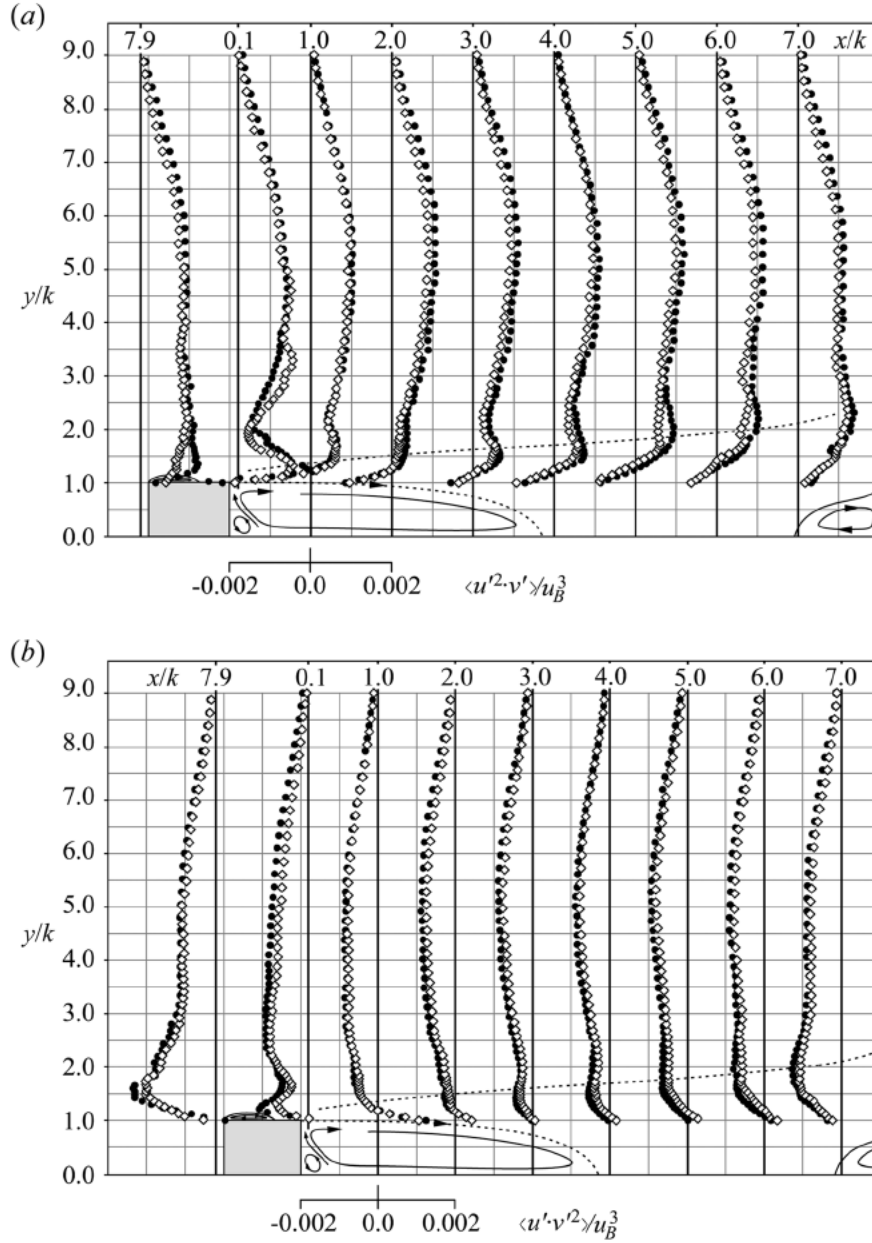


Fig. 4 Normalized triple velocity correlations: (a) $\langle u'^2 v' \rangle$ and (b) $\langle u' v'^2 \rangle$: \diamond $Re_h = 5.0 \times 10^4$ and \bullet $Re_h = 1.0 \times 10^5$. Mean uncertainty in $\langle u'^2 v' \rangle / u_B^3$: ± 0.00014 and ± 0.00016 and in $\langle u' v'^2 \rangle / u_B^3$: ± 0.00009 and ± 0.00010 for $Re_h = 5.0 \times 10^4$ and 1.0×10^5 .

$\langle u' v'^2 \rangle > 0$ indicate the turbulent transport of cold high-momentum fluid from the core flow toward the channel wall, and $\langle u'^2 v' \rangle > 0$ and $\langle u' v'^2 \rangle < 0$ indicate the turbulent transport of low-momentum fluid from the ribbed wall toward the core flow. The alternation of the $\langle u'^2 v' \rangle$ and $\langle u' v'^2 \rangle$ distribution above the rib indicated a large contribution of turbulent diffusion to TKE and Reynolds stress budgets. The global and local minima of $\langle u' v'^2 \rangle$ above the rib leading and trailing edges reflect the strong transport of turbulent flow near the rib. In this region, the generation of highly intense vortices [8] and strong ejection events [10] was found for lower Reynolds number flows, and the presented triple velocity correlations suggest that this is also true for channel flows with Reynolds numbers of up to $Re_H = 1.0 \times 10^5$.

3.2 Quadrant Analysis. Quadrant analysis [38] enables the qualification of ejection and sweep events, which are affected by the roughnesses in rough-wall turbulent boundary layers

[28,30,39] as well as in ribbed channel flows [10,11,32,40], and was applied to the measured velocity field. In general, the intermittent blowout of decelerated fluid at the near-wall region away from the wall is called ejection, while the subsequent downward movement of accelerated fluid is called a sweep. Both events play a significant role for Reynolds stress development near rough and ribbed walls. For a quadrant analysis, the instantaneous Reynolds shear stress at a specified measurement location is classified by the sign of u' and v' into the four categories: outward interaction ($u' > 0, v' > 0$), ejection ($u' < 0, v' > 0$), inward interaction ($u' < 0, v' < 0$), and sweep ($u' > 0, v' < 0$). The four quadrants of a histogram plot (Q_1, \dots, Q_4) of the time-dependent product $u' \cdot v'$ represent these four categories graphically.

3.2.1 Fractional Contribution to $\langle u' v' \rangle$. In this study, the method for determining the fractional contributions from each quadrant to the Reynolds shear stress described by Lu and Willmarth [41] was modified in order to include the residence time

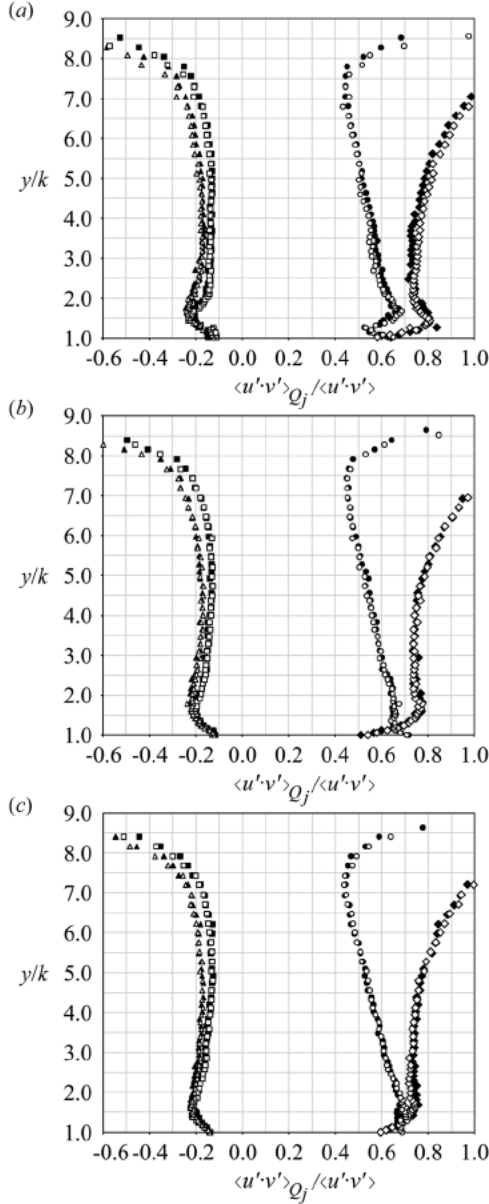


Fig. 5 Contributions (without a hyperbolic hole region) to the Reynolds shear stress behind the rib to the j -th quadrants at (a) $x/k = 0.1$, (b) $x/k = 1.0$, and (c) $x/k = 2.0$. $\text{Re}_h = 5.0 \times 10^4$: \square Q_1 , \diamond Q_2 , \triangle Q_3 , \circ Q_4 ; $\text{Re}_h = 1.0 \times 10^5$: \blacksquare Q_1 , \blacklozenge Q_2 , \blacktriangle Q_3 , \bullet Q_4 .

weighting of the LDA data. The relative contribution to $\langle u'v' \rangle$ from the j th quadrant can be written as

$$\frac{\langle u'v' \rangle_{Q_j}}{\langle u'v' \rangle} = \frac{\sum_i^N (u_i - \langle u \rangle) \cdot (v_i - \langle v \rangle) \cdot \Delta t_i \cdot h_j}{\sum_i^N (u_i - \langle u \rangle) \cdot (v_i - \langle v \rangle) \cdot \Delta t_i} \quad (1)$$

where u_i and v_i are the velocities, and Δt_i is the residence time of the i th particle in the measuring volume. The indicator function is defined as

$$h_j = \begin{cases} 1, & \text{when } u'_i \cdot v'_i \text{ is in the } j\text{th quadrant in the } u\text{-}v\text{-plane} \\ 0, & \text{otherwise} \end{cases}$$

with the velocity fluctuations $u'_i = u_i - \langle u \rangle$ and $v'_i = v_i - \langle v \rangle$ produced by the i th particle.

The quadrant contributions (without a hyperbolic hole region) to the Reynolds shear stress at different streamwise positions behind the rib are depicted in Fig. 5 and in front of the rib in Fig. 6. The contributions were similar for both Reynolds numbers. The presented distributions above $y/k = 3.0$ to 4.0 were almost unaffected by the streamwise position and tend to infinity with increasing wall distance when the Reynolds shear stresses converge to zero. Since $-\langle u'v' \rangle$ was entirely positive in the measurement region, Q_1 and Q_3 were negative and Q_2 and Q_4 were positive. The magnitudes of the relative contributions outside the near-rib region were comparable to those found for flows in a two-dimensional channel with ribbed surfaces [32]. At the ribbed channel wall, Q_2 and Q_4 were many times larger than Q_1 and Q_3 as shown in Figs. 5 and 6, and it is obvious that ejection and sweep events, represented by Q_2 and Q_4 , were the main contributors to the Reynolds shear stress. Their increases corresponded to regions where the deviations of the triple velocity correlations indicated noticeable turbulent diffusion of TKE. Q_2 can be considered as the dominant quadrant for turbulent diffusion near the rib leading edge and above the rib wake indicating turbulent transport of energy from the ribbed wall toward the core flow. The Q_2 peak behind the rib trailing edge (Figs. 5(a) and 5(b)) corresponded to intense ejection events. Their occurrence was in accordance with the unsteady bursts in this region as shown by Cardwell et al. [11]. Turbulent flow structures coming from the separated shear layer were ejected outwards entraining fluid from the beneath located recirculation region. Except for the locally restricted ejection events near the rib, turbulent transport behind the rib was driven by the flapping motion of the shear layer as expected from the triple velocity correlations in Figs. 3 and 4. Rotational fluid that developed within the shear layer or was entrained as a result of shear layer movement was ejected outwards or swept wallwards. Therefore, the portion of sweep events to the transport of the Reynolds shear stress increased toward the ribbed channel wall, while Q_2 decreased and Q_2 peaks drifted outward further downstream (Figs. 5(b) and 5(c)). The increase in Q_4 agreed with the near-wall decrease of $\langle u'^2 v' \rangle$ and increase of $\langle u'v'^2 \rangle$ (Fig. 4). The nearly uniform distributions of Q_2 and Q_4 in the region between $x/k = 3.0$ and $x/k = 6.0$ showed that no unsteady transport phenomena other than the shear layer flapping contributed to the Reynolds shear stress. The contributions from the interaction-associated quadrants were similar behind the ribs and remained nearly unchanged for $x/k = 1.0$ and 2.0 , and thus it can be concluded that the increase in Q_4 was balanced by the reduction of Q_2 .

Since the generator for ejection and sweep events within the inter rib-spacing was the flapping shear layer, Q_2 and Q_4 close to $y = 1.0$ became slightly weaker further downstream (Figs. 5(b), 5(c), and 6(a)). Toward the subsequent rib, local peaks of each quadrant were smoothed out as shown in Figs. 6(a) and 6(b). With the onset of the upward fluid motion at $x/k = 7.0$, the Q_2 contributions increased, while the Q_4 contributions remained unaffected (Figs. 6(b) and 6(c)). Substantial enhancements of sweep and ejection events at the rib leading edge were accompanied by an increase in the Q_1 and Q_3 contributions. Similarly to lower Reynolds number flows [10], it is apparent that ejection events are significant for the flow near-rib leading edge at Reynolds numbers of $\text{Re}_h = 5.0 \times 10^4$ and 1.0×10^5 and, therefore, have a large impact for the relevant momentum and heat transport of the cooling designs of ribbed surfaces. It is supposed that the ejection events above the rib leading edge were mostly generated with bursts of flow structures which originated in an inclined shear layer and the small recirculation region in front of the windward rib surface: Driven by the intermittent impingement process of the flow structures that shed from the previous rib, the inclined shear layer becomes unstable and breaks up from time to time. During the shear layer disruption, rotational fluid from the beneath located recirculation region is ejected outwards. The outward fluid motion is intensified by upward directed convective transport due to the rib blockage. At the rib crest, the ejected fluid interacts with the fluid entrapped in the small recirculation zone near the rib leading

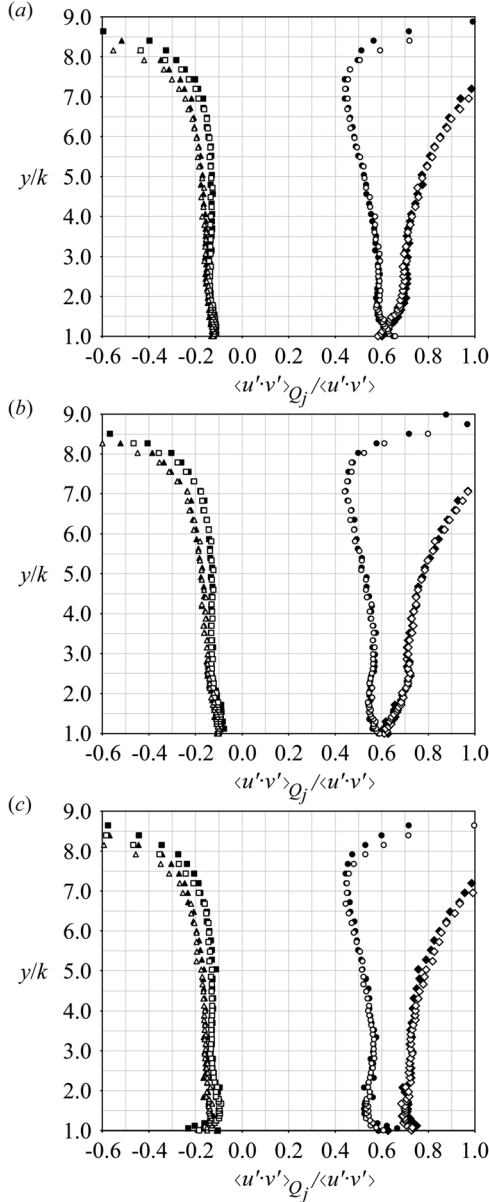


Fig. 6 Contributions (without a hyperbolic hole region) to the Reynolds shear stress in front of the rib to the j -th quadrants at (a) $x/k = 6.0$, (b) $x/k = 7.0$, and (c) $x/k = 7.9$. $\text{Re}_h = 5.0 \times 10^4$: \square Q_1 , \diamond Q_2 , \triangle Q_3 , \circ Q_4 ; $\text{Re}_h = 1.0 \times 10^5$: \blacksquare Q_1 , \blacklozenge Q_2 , \blacktriangle Q_3 , \bullet Q_4 .

edge and strengthens before it bursts away. In this case, the intensity of the ejection events would be significantly affected by the development of the recirculation region on the rib crest and would therefore depend on the rib height and width as well as the relative roughness. Bimodal probability distributions of the velocities found immediately above the rib crest in the vicinity of the rib leading edge by Mullin and Martin [23] support the assumption that the fluid in recirculation region at the rib crest contributes to the burst process.

3.2.2 Contributions from Intense Fluctuations. By applying the concept of Willmarth and Lu [42] for a hyperbolic hole with the hole size parameter $H = |u' \cdot v'| / |\langle u'v' \rangle|$ to the quadrant analysis, the contribution to $\langle u'v' \rangle$ from intense fluctuations $u' \cdot v'$ can be extracted. For considering the residence time weighting of the LDA measurement data, the concept was extended. Therefore, the contributions to $\langle u'v' \rangle$ from the different events at one measurement point were determined from

$$\langle u'v' \rangle_{Q_j} = \frac{\sum_i^N u'_i \cdot v'_i \cdot \Delta t_i \cdot n_j(H_{\Delta t})}{\sum_i^N \Delta t_i} \quad (2)$$

with the indicator function

$$n_j(H_{\Delta t}) = \begin{cases} 1, & \text{when } |q_{uv_i}| > |\langle u'v' \rangle| \cdot H_{\Delta t} \text{ and } u'_i \cdot v'_i \\ & \text{is in } j\text{th quadrant in the } u\text{-}v\text{-plane} \\ 0, & \text{otherwise} \end{cases}$$

the residence time-weighted relative contribution

$$q_{uv_i} = \frac{u'_i \cdot v'_i \cdot \Delta t_i}{\sum_i^N \Delta t_i}$$

and the range of the relative hole size

$$H_{\Delta t} = [0, \dots, \max\{|q_{uv_i}| / |\langle u'v' \rangle|\}]$$

The presented method of a relative hole size enables a qualitative analysis of the occurrence of intense events that contribute to the Reynolds shear stress. The fractional contributions from each quadrant to the Reynolds shear stress for an increasing relative hole size at different locations are shown in Fig. 7. The relative hole size was normalized by the value when the contribution from the hole region reached 1. The distributions of each contribution showed no particular Reynolds number dependence regardless of the measuring point in the entire measuring range. In accordance with Figs. 5 and 6, Q_2 and Q_4 were the main contributors, while the contributions from Q_1 and Q_3 were comparatively small. Above the rib leading and trailing edges close to the peaks of Q_2 (Figs. 7(a), 7(b), 7(e), and 7(f)), the predominance of ejection events for generating large Reynolds shear stress remained with increasing relative hole size. Except for the regions where bursts dominated the flow motion, the intensity of sweep events contributing to the Reynolds shear stress increased toward the ribbed channel wall. Nevertheless, within the inter-rib spacing from $x/k = 0.0$ to 7.0 and around $y/k = 1.0$ (Figs. 7(c) and 7(d)), it was found that sweep events contributed with lower intensity than ejection events. For a relative hole size larger than 0.3 at $\text{Re}_h = 5.0 \times 10^4$ and 0.5 at $\text{Re}_h = 5.0 \times 10^4$, the only contributions came from Q_2 and from the hole region. Therefore, ejection events contributed with high intensity to the Reynolds shear stress above $y/k = 1.0$, while sweep events produced less turbulent shear. This finding is in contrast to rough-wall turbulent boundary layer flows [28,30,31] or the flows in a two-dimensional channel with ribbed surfaces [32] of lower relative roughness, where the Q_2 contribution for strong events was found to be comparably small. It could be assumed that the difference compared to rough-wall turbulent boundary layer or two-dimensional channel flows in the significance of high-intense sweep events for the Reynolds shear stress generation originates in the three-dimensionality of the main secondary flow structures which develop in the square ribbed channel. The secondary flow in square ribbed channels induces a steady downward directed fluid motion above the ribs near the channel center plane which limits the vertical growth of the separated shear layer leading to a flat downstream propagation of its flow structures. High-intense sweep events originating in the shear layer flapping are less pronounced in the environment of the steady downward directed flow above $y/k = 1.0$ within the inter-rib spacing. Their occurrence is restricted to a region below the rib height where the secondary flow motion is weakened. This assumption is supported by the small increase in Q_4 (Figs. 5 and 6) near the ribbed channel wall and the zero-crossing of $\langle v^3 \rangle$ below and of $\langle u'v^2 \rangle$ close to $y/k = 1.0$.

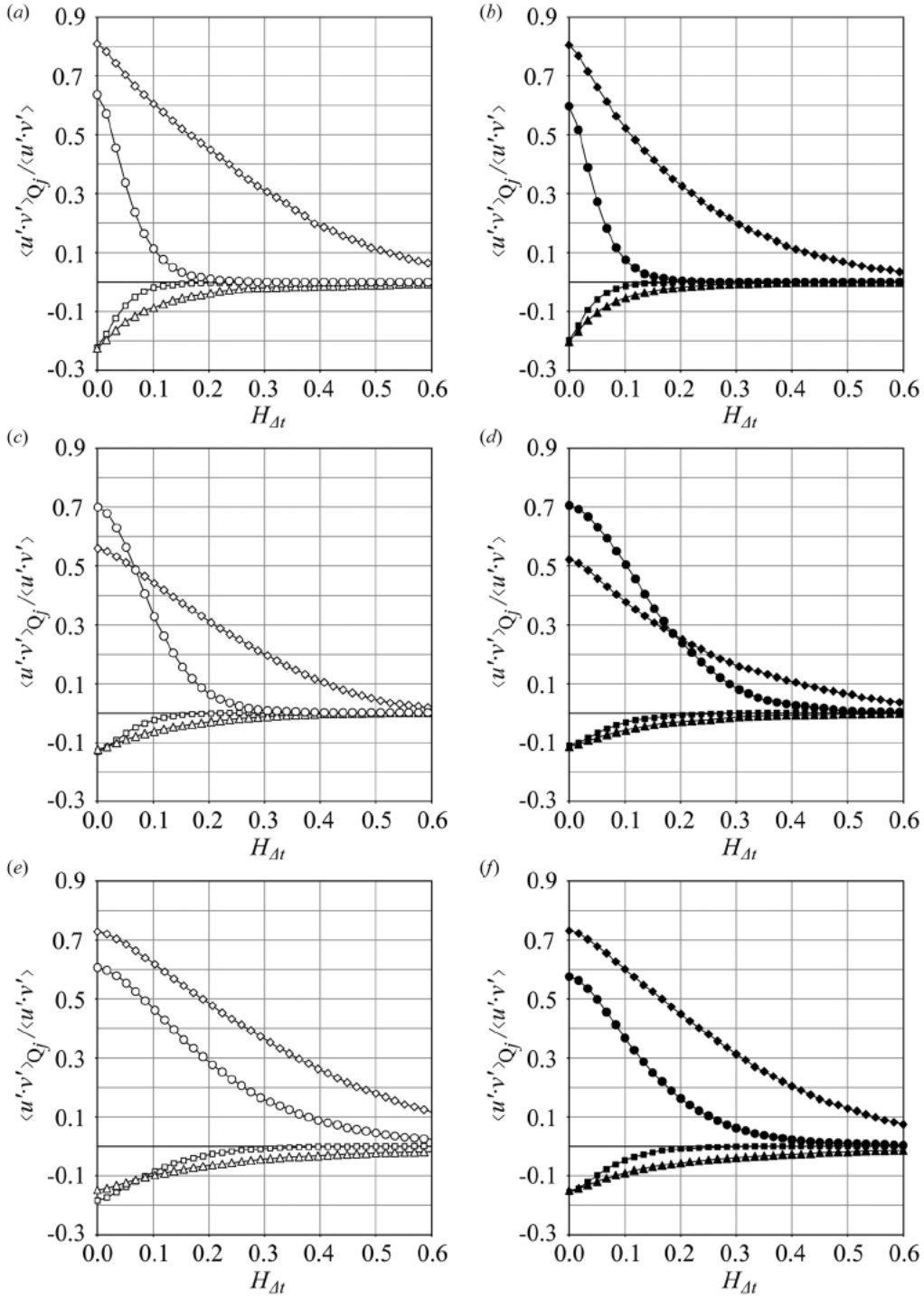


Fig. 7 Contributions to the Reynolds shear stress from different events for increasing normalized relative hole size $H_{\Delta t,n}$. (a) and (b): $x/k = 0.1$, $y/k = 1.35$; (c) and (d): $x/k = 1.0$, $y/k = 1.03$; (e) and (f): $x/k = 7.9$, $y/k = 1.01$. $Re_h = 5.0 \times 10^4$: \square Q_1 , \diamond Q_2 , \triangle Q_3 , \circ Q_4 ; $Re_h = 1.0 \times 10^5$: \blacksquare Q_1 , \blacklozenge Q_2 , \blacktriangle Q_3 , \bullet Q_4 .

4 Conclusions

Velocity measurements in a one-sided ribbed square channel were performed to investigate the turbulent transport at Reynolds numbers of $Re_h = 5.0 \times 10^4$ and 1.0×10^5 . Although the measurements were restricted to only the channel center plane and three-dimensional effects from the cross-stream flow cannot be inferred, the presented results pointed out the crucial role of turbulent transport for fluid mixing in the proximity of the rib. The transport of Reynolds normal stress by velocity fluctuations

behind the rib occurred with streamwise-elongated flow structures which developed during the shedding process. The highly unsteady flow structures shed from the rib caused the vertical flux of Reynolds shear stress which is supposed to contribute largely to the TKE. A frequent occurrence of strong sweep events within the flapping shear layer behind the rib was detected, while strong ejection events were found at the rib leading edge and immediately above the recirculation region behind the rib in the presented Reynolds number range. In accordance with former studies [8,10,11], ejection events contributed intensely to the Reynolds

shear stress and are of great importance to the turbulent transport in the flow field of square ribbed channels. The strong ejection events at the rib leading edge were attributed to bursting flow structures that originated in the inclined shear layer and the beneath located small recirculation region in front of the rib and interacted with the recirculating fluid at the rib crest. The presented results highlighted the importance of turbulent transport for the computations used in the design of rib-roughened cooling channels. Since the streamwise-vertical Reynolds shear stress correlates strongly with the local heat transfer in ribbed channels [9], it is apparent that turbulent transport is significant for thermal considerations of ribbed cooling channels and relevant for computations of thermal turbulent flow in similarly structured ducts.

In general, ejection and sweep events were the main contributors to the Reynolds shear stress. Although sweep events predominated near the ribbed channel wall, it was found that ejection events contributed with higher intensity to the Reynolds shear stress. The absence of the high-intense ejection events for the Reynolds shear stress generation of turbulent flows in two-dimensional channel configurations highlighted the effect of the secondary flow motion shaped three-dimensional flow field on the turbulent transport mechanism in square ribbed channels. It is supposed that the downwards directed steady fluid motion from the secondary flow above the ribbed wall suppresses a well pronounced occurrence of high-intense sweep events and restricts them spatially to a region below the rib height.

The turbulent transport phenomena revealed by triple velocity correlations and quadrant analysis were almost Reynolds number-insensitive and, thus, exhibit some similarities to flows in square channel at lower Reynolds numbers and higher or lower relative roughness [8,11,13,23,27,40]. Therefore, it can be concluded that the turbulent transport indicated by the triple velocity correlations in ribbed channels with similar geometrical parameters like in this study shows comparable mechanisms for Reynolds numbers of up to $Re_H = 1.0 \times 10^5$. The Reynolds number-insensitivity of the turbulent transport can support the use of scale-resolving simulation methods in the design process of rib roughnesses for structuring the fluid–solid interfaces of heat exchange applications. Due to the enormously high computational demand of scale-resolving simulation methods, their application in geometric parameter studies for the thermal-hydraulic design of rib structures at Reynolds numbers relevant to high-temperature cooling applications is currently limited. According to the Reynolds number-insensitivity, it would be suggested to examine to what extent a transfer of the results obtained at the lowest possible Reynolds number to higher Reynolds number ranges is possible. Within the given Reynolds number range, geometry modifications of rib structures could be investigated first for small Reynolds numbers at reduced computational cost. Subsequently, the results would be confirmed at higher, application-relevant Reynolds numbers.

Nomenclature

b = rib width
 h = channel height
 H = hole size parameter
 h_j = indicator function
 $H_{\Delta t}$ = range of the relative hole size
 k = rib height
 \dot{m} = mass flow rate
 N = sample number at each measurement location
 n_j = indicator function
 p = pitch
 p_{in} = inlet pressure
 q_{uv_i} = residence time-weighted relative contribution
 Q_1 = quadrant analysis: outward interaction
 Q_2 = quadrant analysis: ejection event
 Q_3 = quadrant analysis: inward interaction
 Q_4 = quadrant analysis: sweep event
 Re_h = Reynolds number, $u_B \cdot h/\nu = \dot{m} \cdot \mu(T_{in})^{-1} \cdot h^{-1}$

T_{in} = inlet temperature
TKE = turbulence kinetic energy
 u' = instantaneous streamwise velocity fluctuation
 $\langle u \rangle$ = mean streamwise velocity
 $\langle u'v' \rangle$ = Reynolds shear stress
 u_B = bulk velocity
 $\langle u'^3 \rangle$ = triple velocity correlation
 $\langle u'^2v' \rangle$ = triple velocity correlation
 $\langle u'v'^2 \rangle$ = triple velocity correlation
 v' = instantaneous vertical velocity fluctuation
 $\langle v \rangle$ = mean vertical velocity
 $\langle v'^3 \rangle$ = triple velocity correlation
 w = channel width
 x = streamwise direction
 y = vertical direction
 z = spanwise direction
 Δt_i = residence time of the i th particle
 μ = dynamic viscosity
 ν = kinematic viscosity

References

- [1] Han, J.-C., 2004, "Recent Studies in Turbine Blade Cooling," *Int. J. Rotating Mach.*, **10**(6), pp. 443–457.
- [2] Ruck, S., Arbeiter, F., Brenneis, B., Hernandez, F., Neuberger, H., and Schwab, F., 2019, "Thermal-Hydraulic Study on Rib and Dimple Structures for Cooling the First Wall of DEMO," *Fusion Eng. Des.*, **146**, pp. 2144–2148.
- [3] Bhushan, B., and Singh, R., 2010, "A Review on Methodology of Artificial Roughness Used in Duct of Solar Air Heaters," *Energy*, **35**(1), pp. 202–212.
- [4] Tanda, G., 2011, "Performance of Solar Air Heater Ducts With Different Types of Ribs on the Absorber Plate," *Energy*, **36**(11), pp. 6651–6660.
- [5] Liou, T. M., Hwang, J. J., and Chen, S. H., 1992, "Turbulent Transport Phenomena in a Channel With Periodic Rib Turbulators," *J. Thermophys. Heat Transfer*, **6**(3), pp. 513–521.
- [6] Rau, G., Cakan, M., Moeller, D., and Arts, T., 1998, "The Effect of Periodic Ribs on the Local Aerodynamic and Heat Transfer Performance of a Straight Cooling Channel," *ASME J. Turbomach.*, **120**(2), pp. 368–375.
- [7] Graham, A., Sewall, E., and Thole, K. A., 2004, "Flowfield Measurements in a Ribbed Channel Relevant to Internal Turbine Blade Cooling," *ASME Paper No. GT2004-53361*.
- [8] Mahmoodi-Jezeh, S. V., and Wang, B.-C., 2020, "Direct Numerical Simulation of Turbulent Flow Through a Ribbed Square Duct," *J. Fluid Mech.*, **900**, p. A18.
- [9] Casarsa, L., and Arts, T., 2005, "Experimental Investigation of the Aerothermal Performance of a High Blockage Rib-Roughened Cooling Channel," *ASME J. Turbomach.*, **127**(3), pp. 580–588.
- [10] Wang, L., Salewski, M., and Sundén, B., 2010, "Turbulent Flow in a Ribbed Channel: Flow Structures in the Vicinity of a Rib," *Exp. Therm. Fluid Sci.*, **34**(2), pp. 165–176.
- [11] Cardwell, N. D., Vlachos, P. P., and Thole, K. A., 2011, "Developing and Fully Developed Turbulent Flow in Ribbed Channels," *Exp. Fluids*, **50**(5), pp. 1357–1371.
- [12] Coletti, F., Maurer, T., Arts, T., and Di Sante, A., 2012, "Flow Field Investigation in Rotating Rib-Roughened Channel by Means of Particle Image Velocimetry," *Exp. Fluids*, **52**(4), pp. 1043–1061.
- [13] Coletti, F., Cresci, I., and Arts, T., 2013, "Spatio-Temporal Analysis of the Turbulent Flow in a Ribbed Channel," *Int. J. Heat Fluid Flow*, **44**, pp. 181–196.
- [14] Coletti, F., Jacono, D. L., Cresci, I., and Arts, T., 2014, "Turbulent Flow in Rib-Roughened Channel Under the Effect of Coriolis and Rotational Buoyancy Forces," *Phys. Fluids*, **26**(4), p. 045111.
- [15] Ruck, S., and Arbeiter, F., 2021, "LDA Measurements in a One-Sided Ribbed Square Channel at Reynolds Numbers of 50,000 and 100,000," *Exp. Fluids*, **62**, p. 232.
- [16] Sewall, E. A., Tafti, D. K., Graham, A. B., and Thole, K. A., 2006, "Experimental Validation of Large Eddy Simulations of Flow and Heat Transfer in a Stationary Ribbed Duct," *Int. J. Heat Fluid Flow*, **27**(2), pp. 243–258.
- [17] Labbé, O., 2013, "Large-Eddy-Simulation of Flow and Heat Transfer in a Ribbed Duct," *Comput. Fluids*, **76**, pp. 23–32.
- [18] Mahmoodi-Jezeh, S. V., and Wang, B.-C., 2021, "Direct Numerical Simulation of Turbulent Heat Transfer in a Square Duct With Transverse Ribs Mounted on One Wall," *Int. J. Heat Fluid Flow*, **89**, p. 108782.
- [19] Lohász, M. M., Rambaud, P., and Benocci, C., 2006, "Flow Features in a Fully Developed Ribbed Duct Flow as a Result of MILES," *Flow, Turbul. Combust.*, **77**(1–4), pp. 59–76.
- [20] Yokosawa, H., Fujita, H., Hirota, M., and Iwata, S., 1989, "Measurement of Turbulent Flow in a Square Duct With Roughened Walls on Two Opposite Sides," *Int. J. Heat Fluid Flow*, **10**(2), pp. 125–130.
- [21] Fujita, H., Yokosawa, H., and Hirota, M., 1989, "Secondary Flow of the Second Kind in Rectangular Ducts With One Rough Wall," *Exp. Therm. Fluid Sci.*, **2**(1), pp. 72–80.
- [22] Hirota, M., Yokosawa, H., and Fujita, H., 1992, "Turbulence Kinetic Energy in Turbulent Flows Through Square Ducts With Rib-Roughened Walls," *Int. J. Heat Fluid Flow*, **13**(1), pp. 22–29.

- [23] Mullin, T., and Martin, S. R., 1991, "Intermittent Phenomena in the Flow Over a Rib Roughened Surface," *ASME J. Fluids Eng.*, **113**(2), pp. 206-209.
- [24] Islam, M. S., Haga, K., Kaminaga, M., Hino, R., and Monde, M., 2002, "Experimental Analysis of Turbulent Flow Structure in a Fully Developed Rib-Roughened Rectangular Channel With PIV," *Exp. Fluids*, **33**(2), pp. 296-306.
- [25] Liou, T., Wu, Y., and Chang, Y., 1993, "LDV Measurements of Periodic Fully Developed Main and Secondary Flows in a Channel With Rib-Disturbed Walls," *ASME J. Fluids Eng.*, **115**(1), pp. 109-114.
- [26] Wang, L., Hejicik, J., and Sundén, B., 2007, "PIV Measurement of Separated Flow in a Square Channel With Streamwise Periodic Ribs on One Wall," *ASME J. Fluids Eng.*, **129**(7), pp. 834-841.
- [27] Fang, X., Yang, Z., Wang, B. C., Tachie, M. F., and Bergstrom, D., 2017, "Large-Eddy Simulation of Turbulent Flow and Structures in a Square Duct Roughened With Perpendicular and V-Shaped Ribs," *Phys. Fluids*, **29**(6), p. 065110.
- [28] Krogstad, P., and Antonia, R., 1999, "Surface Roughness Effects in Turbulent Boundary Layers," *Exp. Fluids*, **27**(5), pp. 450-460.
- [29] Antonia, R. A., and Krogstad, P., 2001, "Turbulence Structure in Boundary Layers Over Different Types of Surface Roughness," *Fluid Dyn. Res.*, **28**(2), pp. 139-157.
- [30] Keirsbulck, L., Labraga, L., Mazouz, A., and Toumier, C., 2002, "Surface Roughness Effects on Turbulent Boundary Layer Structures," *ASME J. Fluids Eng.*, **124**(1), pp. 127-135.
- [31] Krogstad, P., and Efros, V., 2012, "About Turbulence Statistics in the Outer Part of a Boundary Layer Developing Over Two-Dimensional Surface Roughness," *Phys. Fluids*, **24**(7), p. 075112.
- [32] Krogstad, P.-Å., Andersson, H. I., Bakken, O. M., and Ashrafian, A., 2005, "An Experimental and Numerical Study of Channel Flow With Rough Walls," *J. Fluid Mech.*, **530**, pp. 327-352.
- [33] Ikeda, T., and Durbin, P., 2007, "Direct Simulations of a Rough-Wall Channel Flow," *J. Fluid Mech.*, **571**, pp. 235-263.
- [34] George, W. K., Beuther, P. D., and Lumley, J. L., 1978, "Processing of Random Signals," *Proceedings of the Dynamic Flow Conference 1978 on Dynamic Measurements in Unsteady Flows*, B. W. Hansen, ed., Proceedings of the Dynamic Flow Conference 1978 on Dynamic Measurements in Unsteady Flows, Marseille, Sept. 11-14, Baltimore, Sept. 18-21, Springer, Dordrecht, The Netherlands, pp. 757-800.
- [35] Benedict, L., and Gould, R., 1996, "Towards Better Uncertainty Estimates for Turbulence Statistics," *Exp. Fluids*, **22**(2), pp. 129-136.
- [36] Tennekes, H., and Lumley, J. L., 1972, *A First Course in Turbulence*, MIT Press, Cambridge, MA/London.
- [37] Hanjalić, K., and Launder, B. E., 1972, "Fully Developed Asymmetric Flow in a Plane Channel," *J. Fluid Mech.*, **51**(2), pp. 301-335.
- [38] Wallace, J. M., Eckelmann, H., and Brodkey, R. S., 1972, "The Wall Region in Turbulent Shear Flow," *J. Fluid Mech.*, **54**(1), pp. 39-48.
- [39] Raupach, M. R., 1981, "Conditional Statistics of Reynolds Stress in Rough-Wall and Smooth-Wall Turbulent Boundary Layers," *J. Fluid Mech.*, **108**, pp. 363-382.
- [40] Fang, X., Yang, Z., Wang, B. C., Tachie, M. F., and Bergstrom, D. J., 2015, "Highly-Disturbed Turbulent Flow in a Square Channel With V-Shaped Ribs on One Wall," *Int. J. Heat Fluid Flow*, **56**, pp. 182-197.
- [41] Lu, S. S., and Willmarth, W. W., 1973, "Measurements of the Structure of the Reynolds Stress in a Turbulent Boundary Layer," *J. Fluid Mech.*, **60**(3), pp. 481-511.
- [42] Willmarth, W. W., and Lu, S. S., 1972, "Structure of the Reynolds Stress Near the Wall," *J. Fluid Mech.*, **55**(1), pp. 65-92.